Uniform Strain Elements for Three-Node Triangular and Four-Node Tetrahedral Meshes [1]

C. R. Dohrmann[2]

M. W. Heinstein[3]

J. Jung[3]

S. W. Key[3]

W. R. Witkowski[2]

Abstract. A family of uniform strain elements is presented for three-node triangular and four-node tetrahedral meshes. The elements use the linear interpolation functions of the original mesh, but each element is associated with a single node. As a result, a favorable constraint ratio for the volumetric response is obtained for problems in solid mechanics. The uniform strain elements do not require the introduction of additional degrees of freedom and their performance is shown to be significantly better than that of three-node triangular or four-node tetrahedral elements. In addition, nodes inside the boundary of the mesh are observed to exhibit superconvergent behavior for a set of example problems.

---

[2]Structural Dynamics Department, Sandia National Laboratories, MS 0439, Albuquerque, New Mexico 87185-0439, email: crdohrm@sandia.gov, phone: (505) 844-8058, fax: (505) 844-9297.

[3]Engineering and Manufacturing Mechanics Department, Sandia National Laboratories, MS 0443, Albuquerque, New Mexico 87185-0443.

DISCLAIMER

DISCLAIMER

Portions of this document may be illegible in electronic image products. Images are produced from the best available original document.

1. Introduction

Owing to their simplicity, the three-node triangle and four-node tetrahedron are often used in textbooks to introduce the finite element method in two and three dimensions. These elements are based on piecewise linear approximations that interpolate responses at the nodes of the mesh. Because linear approximations are used, the spatial derivatives of the responses are constant within each element. As a result, the elements can be implemented very efficiently in finite element programs. Moreover, many automatic meshing programs are based on creating triangular or tetrahedral elements.

Although the three-node triangle and four-node tetrahedron have several advantages, they also possess significant shortcomings for problems in solid mechanics. One such shortcoming is volumetric locking [1]. Meshes of tetrahedral elements or triangular elements in plane strain often behave much too stiffly for nearly incompressible materials. Consequently, an unreasonably large number of elements may be required to obtain satisfactory results. For this reason and others, the linear triangle and tetrahedron are often avoided in practice.

Volumetric locking of finite elements can be reduced or eliminated altogether using a variety of different approaches. One approach is to use higher-order interpolation functions for the elements. The six-node triangle and ten-node tetrahedron use quadratic interpolation functions and avoid many of the shortcomings of their constant strain counterparts. Another approach is to adopt a mixed formulation for the elements where pressure is used as a variable in addition to displacement. A third approach is to employ uniform reduced integration or selective reduced integration. The basic idea of reduced integration schemes is to numerically integrate the volumetric strain energy with a lower-order quadrature rule than

is used conventionally. Unfortunately, this approach cannot be applied to the three-node triangle or four-node tetrahedron since both elements already use the simplest quadrature rule possible.

The underlying cause of volumetric locking for the three-node triangle and four-node tetrahedron is the presence of too many constraints for incompressible materials. As an illustration, consider a square mesh of four-node quadrilateral elements in plane strain with n elements per edge. The use of single-point integration for the volumetric strain energy imposes a constraint of zero volume change for each element. Thus, the total number of constraints is n^2, but this number is not large enough to cause volumetric locking. If, however, a four-point quadrature rule is used, then additional constraints are introduced and the mesh will lock. A similar situation arises if each quadrilateral is replaced by two triangles. In this case, there are $2n^2$ volume constraints as opposed to n^2. Taken together, these constraints severely restrict the range of possible deformations of the triangular mesh.

The constraint ratio for volumetric response [1] is a simple measure used for determining the ability of an element to perform well in incompressible and nearly incompressible applications. Stated simply, the constraint ratio is the ratio of the number of available degrees of freedom to the number of incompressibility constraints. In the case of the quadrilateral mesh cited above, this ratio is given by $2(n + 1)^2/n^2$ (omitting boundary conditions). For large values of n this ratio approaches the optimal value of 2. In three dimensions, the optimal value of the constraint ratio is 3. The uniform strain elements presented in this study use the interpolation functions of the original mesh, but each of the new "elements" is associated with just a single node. As a result, optimal constraint ratios of 2 and 3 are obtained for problems in two and three dimensions.

2

The idea of associating elements (cells) with nodes is also used by finite volume [2] (FV) and finite volume element [3-5] (FVE) methods. These methods are sometimes referred to as cell-centered finite differences and generalized box methods, respectively. To help explain some of the similarities and differences between FV, FVE, standard finite element (FE), and the present uniform strain (US) approach, consider the mesh of three-node equilateral triangles shown in Figure 1. Dashed lines in the figure are formed by triangle edge perpendicular bisectors and serve as element (cell) boundaries for FV, FVE and US. Based on results presented in References 4 and 6, the coefficient matrix K for approximate solutions to Poisson's equation on this mesh is identical for FV, FVE and FE. In contrast, K is different for US. To be specific, let $k_{q,r}$ denote the value in row q and column r of K. The values of $k_{12,20}$, $k_{18,20}$ and $k_{25,20}$ are all zero for FV, FVE and FE, but they are nonzero for US. Similar differences for the problems presented in Section 4 can lead to significant performance differences between US and FE.

The uniform strain elements are based on concepts developed for the quadrilateral and hexahedron [7] and extensions to other element types [8-9]. The elements do not require the introduction of additional degrees of freedom and their performance is shown to be significantly better than that of three-node triangular or four-node tetrahedral elements. In addition, nodes inside the boundary of the mesh are observed to exhibit superconvergent behavior for a set of example problems. The element formulations are quite simple and are presented in Sections 2 and 3. Example problems demonstrating the performance of the elements are provided in Section 4.

2. Element Formulation in Three Dimensions

Consider a mesh of four-node tetrahedral elements numbered from 1 to N_e. Nodal coordinates and nodal displacements are denoted by x_{iI} and u_{iI}, respectively, for $i = 1, 2, 3$ and $I = 1, \ldots, N$. The node numbers for element number J are denoted by J_1, J_2, J_3 and J_4. The volume V_J of element number J can be expressed as

$$V_J = \frac{1}{6} \det \begin{bmatrix} 1 & x_{1J_1} & x_{2J_1} & x_{3J_1} \\ 1 & x_{1J_2} & x_{2J_2} & x_{3J_2} \\ 1 & x_{1J_3} & x_{2J_3} & x_{3J_3} \\ 1 & x_{1J_4} & x_{2J_4} & x_{3J_4} \end{bmatrix} \tag{1}$$

For each tetrahedral element, define (see Ref. 7)

$$B_{Jik} = \partial V_J / \partial x_{iJ_k} \tag{2}$$

Substituting Eq. (1) into Eq. (2), one obtains

$$B_{J11} = [(x_{2J_3} - x_{2J_4})(x_{3J_2} - x_{3J_4}) - (x_{2J_2} - x_{2J_4})(x_{3J_3} - x_{3J_4})]/6 \tag{3}$$

$$B_{J12} = [(x_{2J_1} - x_{2J_3})(x_{3J_1} - x_{3J_4}) - (x_{2J_1} - x_{2J_4})(x_{3J_1} - x_{3J_3})]/6 \tag{4}$$

$$B_{J13} = [(x_{2J_1} - x_{2J_4})(x_{3J_1} - x_{3J_2}) - (x_{2J_1} - x_{2J_2})(x_{3J_1} - x_{3J_4})]/6 \tag{5}$$

$$B_{J14} = [(x_{2J_1} - x_{2J_2})(x_{3J_1} - x_{3J_3}) - (x_{2J_1} - x_{2J_3})(x_{3J_1} - x_{3J_2})]/6 \tag{6}$$

Similar expressions are obtained for the terms B_{J2k} and B_{J3k} by cyclic permutation of the first subscripted index on the right hand sides of Eqs. (3-6). It follows from Eqs. (1) and (3-6) that

$$V_J = \sum_{k=1}^{4} x_{iJ_k} B_{Jik} \qquad i = 1, 2, 3 \tag{7}$$

The basic idea of the following development is to associate new elements with each of the nodes of the mesh. These elements use the interpolation functions of the original mesh, but

4

their formulation is different from the four-node tetrahedron. Let $\hat{V}_L$ denote the "volume" of node number L which is defined as

$$\hat{V}_L = \sum_{J=1}^{N_e} \alpha_{LJ} V_J \qquad (8)$$

where α_{LJ} are scalar constants. For the purposes of this study, α_{LJ} is nonzero only if L equals J_1, J_2 or J_3. In other words, α_{LJ} is zero if node number L is not associated with element number J. The constants in Eq. (8) are chosen to satisfy the constraint equation

$$\alpha_{J_1 J} + \alpha_{J_2 J} + \alpha_{J_3 J} + \alpha_{J_4 J} = 1 \qquad (9)$$

for $J = 1, \ldots, N_e$. Satisfaction of Eq. (9) ensures that the volume of each element in the original tetrahedral mesh is accounted for properly.

Two options are considered for selecting the coefficients $\alpha_{J_k J}$. For Option 1,

$$\alpha_{J_k J} = 1/4 \qquad k = 1, \ldots, 4 \qquad (10)$$

and for Option 2,

$$\alpha_{J_k J} = V_{Jk} / (V_{J1} + V_{J2} + V_{J3} + V_{J4}) \qquad k = 1, \ldots, 4 \qquad (11)$$

where V_{Jk} is the volume of the region R_{Jk} inside tetrahedron (J_1, J_2, J_3, J_4) consisting of all points closer to node J_k than to the other three nodes of the tetrahedron. If the tetrahedralization of the nodes in the mesh is Delaunay, then the volume associated with each internal node equals the volume of the Voronoi cell for the node [10].

Rather than providing explicit expressions for V_{Jk}, we note that region R_{Jk} can be defined equivalently in terms of seven linear inequality constraints. Let $\mathbf{n}_m$ denote a vector with the

5

same direction as the outward normal to the face of the tetrahedron opposite node J_m. This vector can be expressed in terms of unit vectors $\mathbf{e}_i$ associated with coordinates x_i as

$$\mathbf{n}_m = n_{1m}\mathbf{e}_1 + n_{2m}\mathbf{e}_2 + n_{3m}\mathbf{e}_3 \tag{12}$$

Similarly, the three vectors originating at node J_k and terminating at the other three nodes of the tetrahedron are expressed as

$$\mathbf{r}_{jk} = r_{1jk}\mathbf{e}_1 + r_{2jk}\mathbf{e}_2 + r_{3jk}\mathbf{e}_3 \qquad j = 1,2,3 \tag{13}$$

Region R_{J_k} is then defined by all points (x_1, x_2, x_3) which satisfy the constraints

$$Ax \le b \tag{14}$$

where

$$
A = \begin{bmatrix}
n_{11} & n_{21} & n_{31} \\
n_{12} & n_{22} & n_{32} \\
n_{13} & n_{23} & n_{33} \\
n_{14} & n_{24} & n_{34} \\
r_{11k} & r_{21k} & r_{31k} \\
r_{12k} & r_{22k} & r_{32k} \\
r_{13k} & r_{23k} & r_{33k}
\end{bmatrix}, \quad
x = \begin{bmatrix} x_1 \\ x_2 \\ x_3 \end{bmatrix}, \quad
b = \begin{bmatrix}
n_{11}x_{1J_2} + n_{21}x_{2J_2} + n_{31}x_{3J_2} \\
n_{12}x_{1J_3} + n_{22}x_{2J_3} + n_{32}x_{3J_3} \\
n_{13}x_{1J_4} + n_{23}x_{2J_4} + n_{33}x_{3J_4} \\
n_{14}x_{1J_1} + n_{24}x_{2J_1} + n_{34}x_{3J_1} \\
r_{11k}x_{11k} + r_{21k}x_{21k} + r_{31k}x_{31k} \\
r_{12k}x_{12k} + r_{22k}x_{22k} + r_{32k}x_{32k} \\
r_{13k}x_{13k} + r_{23k}x_{23k} + r_{33k}x_{33k}
\end{bmatrix} \tag{15}
$$

and

$$x_{ijk} = x_{iJ_k} + r_{ijk}/2 \tag{16}$$

The first four rows of Eq. (14) require all points to be inside the tetrahedron. The final three rows require that all points be closer to node J_k than to the other three nodes of the tetrahedron.

Determining the region defined by Eq. (14) is a standard problem of computational geometry involving half-space intersections. Several computer programs are available in the

public domain to find this region and its volume. The program used in this study is based on the Quickhull algorithm [11]. User-callable routines for the Quickhull algorithm are available on the internet from the address `http://www.geom.umn.edu/locate/qhull`.

For each of the new elements, define

$$\hat{B}_{LiI} = \partial \hat{V}_L / \partial x_{iI} \tag{17}$$

Substituting Eqs. (7) and (8) into Eq. (17), one obtains

$$\hat{B}_{LiI} = \sum_{J=1}^{N_e} \alpha_{LJ}(B_{Ji1}\delta_{J_1 I} + B_{Ji2}\delta_{J_2 I} + B_{Ji3}\delta_{J_3 I} + B_{Ji4}\delta_{J_4 I}) \tag{18}$$

and

$$\hat{V}_L = \sum_{I=1}^{N} x_{1I}\hat{B}_{L1I} \tag{19}$$

Based on the uniform strain approach of Ref. 7, the nodal forces f_{iI} associated with the element stresses for node L are given by

$$f_{iI} = \sum_{j=1}^{3} \sigma_{ij}^L \hat{B}_{LjI} \tag{20}$$

where σ_{ij}^L are components of the Cauchy stress tensor (assumed constant throughout the element). The uniform strain ϵ_L^u associated with node L is expressed in terms of nodal displacements as

$$\epsilon_L^u = B_L u \tag{21}$$

where

$$\epsilon_L^u = \begin{bmatrix} \epsilon_{11L}^u & \epsilon_{22L}^u & \epsilon_{33L}^u & \gamma_{12L}^u & \gamma_{23L}^u & \gamma_{31L}^u \end{bmatrix}^T \tag{22}$$

$$B_L = \frac{1}{\hat{V}_L} \begin{bmatrix} \hat{B}_{L11} & 0 & 0 & \hat{B}_{L12} & 0 & 0 & \cdots & \hat{B}_{L1N} & 0 & 0 \\ 0 & \hat{B}_{L21} & 0 & 0 & \hat{B}_{L22} & 0 & \cdots & 0 & \hat{B}_{L2N} & 0 \\ 0 & 0 & \hat{B}_{L31} & 0 & 0 & \hat{B}_{L32} & \cdots & 0 & 0 & \hat{B}_{L3N} \\ \hat{B}_{L21} & \hat{B}_{L11} & 0 & \hat{B}_{L22} & \hat{B}_{L12} & 0 & \cdots & \hat{B}_{L2N} & \hat{B}_{L1N} & 0 \\ 0 & \hat{B}_{L31} & \hat{B}_{L21} & 0 & \hat{B}_{L32} & \hat{B}_{L22} & \cdots & 0 & \hat{B}_{L3N} & \hat{B}_{L2N} \\ \hat{B}_{L31} & 0 & \hat{B}_{L11} & \hat{B}_{L32} & 0 & \hat{B}_{L12} & \cdots & \hat{B}_{L3N} & 0 & \hat{B}_{L1N} \end{bmatrix} \tag{23}$$

and

$$u = \begin{bmatrix} u_{11} & u_{21} & u_{31} & u_{12} & u_{22} & u_{32} & \cdots & u_{1N} & u_{2N} & u_{3N} \end{bmatrix}^T \tag{24}$$

Elements based on the uniform strain approach have the appealing feature that they pass first-order patch tests.

For small deformations of a linear, elastic, isotropic material with Young's modulus E and Poisson's ratio ν, the element stiffness matrix for node L can be expressed as

$$K_L = \hat{V}_L B_L^T D B_L \tag{25}$$

where the material matrix D is given by

$$D = \begin{bmatrix} 2G + \lambda & \lambda & \lambda & 0 & 0 & 0 \\ \lambda & 2G + \lambda & \lambda & 0 & 0 & 0 \\ \lambda & \lambda & 2G + \lambda & 0 & 0 & 0 \\ 0 & 0 & 0 & G & 0 & 0 \\ 0 & 0 & 0 & 0 & G & 0 \\ 0 & 0 & 0 & 0 & 0 & G \end{bmatrix} \tag{26}$$

and

$$G = \frac{E}{2(1+\nu)} \qquad \lambda = \frac{E\nu}{(1+\nu)(1-2\nu)} \tag{27}$$

Element stiffness matrices for the example problems in Section 4 can be calculated as follows:

1. Calculate B_{Jik} for the original tetrahedral elements using Eqs. (3-6).

2. Calculate $\alpha_{J_k J}$ using Eq. (10) or Eq. (11).

3. Calculate $\hat{B}_{LiI}$ and $\hat{V}_L$ using Eqs. (18) and (19).

4. Assemble B_L and calculate K_L using Eqs. (23) and (25).

Notice that a standard finite element analysis using four-node tetrahedral elements requires computations similar to those in Steps 1 and 4. The only additional computations required are those in Steps 2 and 3.

In contrast to other uniform strain elements such as the eight-node hexahedron and four-node quadrilateral, the elements used in the example problems do not require hourglass control [7] to remove singularities from the stiffness matrix. Nevertheless, we have observed the presence of non-physical, low-energy, modes of deformation from eigenanalyses of stiffness matrices. If necessary, these modes can be stiffened effectively using a general method of hourglass control [12]. Such stiffening was not required for the example problems, but it may be necessary for transient dynamic analyses based on lumped mass matrices or static problems with singularities.

3. Element Formulation in Two Dimensions

The element formulation in two dimensions is identical to that in three dimensions with the exception that volume is replaced by area. The area A_J of element number J can be expressed as

$$A_J = \frac{1}{2} \det \begin{bmatrix} 1 & x_{1J_1} & x_{2J_1} \\ 1 & x_{1J_2} & x_{2J_2} \\ 1 & x_{1J_3} & x_{2J_3} \end{bmatrix} \tag{28}$$

Expressions analogous to Eqs. (2-9) are given by

$$B_{Jik} = \partial A_J / \partial x_{iJ_k} \tag{29}$$

$$B_{J11} = (x_{2J_2} - x_{2J_3})/2 \quad B_{J12} = (x_{2J_3} - x_{2J_1})/2 \quad B_{J13} = (x_{2J_1} - x_{2J_2})/2 \tag{30}$$

$$B_{J21} = (x_{1J_3} - x_{1J_2})/2 \quad B_{J22} = (x_{1J_1} - x_{1J_3})/2 \quad B_{J23} = (x_{1J_2} - x_{1J_1})/2 \tag{31}$$

$$A_J = \sum_{k=1}^{3} x_{iJ_k} B_{Jik} \qquad i = 1, 2 \tag{32}$$

9

$$\hat{A}_L = \sum_{J=1}^{N_e} \alpha_{LJ} A_J \qquad L = 1, \ldots, N \tag{33}$$

$$\alpha_{J_1 J} + \alpha_{J_2 J} + \alpha_{J_3 J} = 1 \tag{34}$$

Again, two options are considered for selecting the coefficients $\alpha_{J_k J}$. For Option 1,

$$\alpha_{J_k J} = 1/3 \qquad k = 1, \ldots, 3 \tag{35}$$

and for Option 2,

$$\alpha_{J_k J} = A_{Jk}/(A_{J1} + A_{J2} + A_{J3}) \qquad k = 1, \ldots, 3 \tag{36}$$

where A_{Jk} is the area of region R_{Jk} shown in Figure 2. Points a, b and c are located at the midpoints of the three edges of triangle (J_1, J_2, J_3). The intersection point of the perpendicular bisectors of these edges is denoted by p and has coordinates

$$
\begin{aligned}
x_{1p} = & \; [(x_{1J_1}^2 + x_{2J_1}^2)(x_{2J_2} - x_{2J_3}) + (x_{1J_2}^2 + x_{2J_2}^2)(x_{2J_3} - x_{2J_1}) + \\
& \; (x_{1J_3}^2 + x_{2J_3}^2)(x_{2J_1} - x_{2J_2})]/(4A_J)
\end{aligned}
\tag{37}
$$

$$
\begin{aligned}
x_{2p} = & \; [(x_{1J_1}^2 + x_{2J_1}^2)(x_{1J_3} - x_{1J_2}) + (x_{1J_2}^2 + x_{2J_2}^2)(x_{1J_1} - x_{1J_3}) + \\
& \; (x_{1J_3}^2 + x_{2J_3}^2)(x_{1J_2} - x_{1J_1})]/(4A_J)
\end{aligned}
\tag{38}
$$

Notice that p can be either inside, outside, or on the boundary of the triangle. In addition, all points within R_{Jk} are closer to node J_k than to the other two nodes. If the triangulation of the nodes in the mesh is Delaunay, then the area associated with each internal node equals the area of the Voronoi polygon for the node. If the coordinates of p are replaced by those of the centroid of the triangle, then Eq. (36) simplifies to Eq. (35).

Expressions analogous to Eqs. (17-25) are given by

$$\hat{B}_{LiI} = \partial \hat{A}_L / \partial x_{iI} \tag{39}$$

10

$$\hat{B}_{LiI} = \sum_{J=1}^{N_e} \alpha_{LJ}(B_{Ji1}\delta_{J_1I} + B_{Ji2}\delta_{J_2I} + B_{Ji3}\delta_{J_3I}) \tag{40}$$

$$\hat{A}_L = \sum_{I=1}^{N} x_{1I}\hat{B}_{L1I} \tag{41}$$

$$f_{iI} = h \sum_{j=1}^{2} \sigma_{ij}^L \hat{B}_{LjI} \tag{42}$$

$$\epsilon_L^u = \begin{bmatrix} \epsilon_{11L}^u & \epsilon_{22L}^u & \gamma_{12L}^u \end{bmatrix}^T \tag{43}$$

$$B_L = \frac{1}{\hat{A}_L} \begin{bmatrix} \hat{B}_{L11} & 0 & \hat{B}_{L12} & 0 & \cdots & \hat{B}_{L1N} & 0 \\ 0 & \hat{B}_{L21} & 0 & \hat{B}_{L22} & \cdots & 0 & \hat{B}_{L2N} \\ \hat{B}_{L21} & \hat{B}_{L11} & \hat{B}_{L22} & \hat{B}_{L12} & \cdots & \hat{B}_{L2N} & \hat{B}_{L1N} \end{bmatrix} \tag{44}$$

$$u = \begin{bmatrix} u_{11} & u_{21} & u_{12} & u_{22} & \cdots & u_{1N} & u_{2N} \end{bmatrix}^T \tag{45}$$

$$K_L = h\hat{A}_L B_L^T D B_L \tag{46}$$

where h is the element thickness. The material matrix D for plane strain is given by

$$D = \begin{bmatrix} 2G+\lambda & \lambda & 0 \\ \lambda & 2G+\lambda & 0 \\ 0 & 0 & G \end{bmatrix} \tag{47}$$

and for plane stress

$$D = \frac{E}{1-\nu^2} \begin{bmatrix} 1 & \nu & 0 \\ \nu & 1 & 0 \\ 0 & 0 & (1-\nu)/2 \end{bmatrix} \tag{48}$$

Element stiffness matrices for the example problems in Section 4 can be calculated as follows:

1. Calculate B_{Jik} for the original triangular elements using Eqs. (30) and (31).

2. Calculate α_{J_kJ} using Eq. (35) or Eq. (36).

3. Calculate $\hat{B}_{LiI}$ and $\hat{A}_L$ using Eqs. (40) and (41).

4. Assemble B_L and calculate K_L using Eqs. (44) and (46).

11

4. Example Problems

All the example problems in this section assume small deformations of a linear, elastic, isotropic material with Young's modulus E and Poisson's ratio ν. Element stiffness matrices are calculated using the procedures outlined in the previous two sections. These matrices are then assembled to form the stiffness matrix of the entire mesh. Equivalent nodal forces for distributed loads are calculated using standard procedures for the three-node triangle and four-node tetrahedron since the same interpolation functions are used by the uniform strain elements.

Calculated values of the energy norm of the error are presented for purposes of comparison and for the investigation of convergence rates. The energy norm of the error is a measure of the accuracy of a finite element approximation and is defined as

$$e = \left[\int_{\Omega} (\epsilon^{fe} - \epsilon^{exact})^T D (\epsilon^{fe} - \epsilon^{exact}) dV \right]^{1/2} \tag{49}$$

where Ω denotes the domain of the mesh and ϵ^{fe} and ϵ^{exact} are the finite element and exact strains, respectively. Recall that element strains are associated with the nodes of the mesh with the present formulation. Consequently, finite element strains can be interpolated using the linear interpolation functions of the original triangular or tetrahedral elements. Such an interpolation is used to calculate e for the uniform strain elements.

4.1 Example 1, Plain Strain Bending Static Analysis

The first example is based on a plain strain bending problem presented in Ref. 1 and shown in Figure 3. The displacement boundary conditions for the problem are given by

$$u_1(0,0) = u_2(0,0) = u_1(0,c) = u_1(x_1,0) = 0 \tag{50}$$

12

Nonzero values for the tractions are given by

$$\sigma_{12}(0, x_2) = \sigma_{12}(L, x_2) = P(c^2 - x_2^2)/(2I) \tag{51}$$

and

$$\sigma_{11}(0, x_2) = -PLx_2/I \tag{52}$$

where P is a given constant and $I = 2c^3/3$. The number of element edges in the horizontal and vertical directions of the mesh equals $2n$ and n, respectively. Thus, the meshes shown in Figure 3 have $n = 4$.

A problem with dimensions $L = 16$ and $c = 2$ is considered first. Results are presented for the uniform strain elements with Option 1 ($UT3^1$) and Option 2 ($UT3^2$), the standard three-node triangle ($T3$), the standard four-node quadrilateral with 2-point iterated Gaussian quadrature ($Q4$), and the four-node quadrilateral with reduced selective integration ($SQ4$). Note that element type $SQ4$ is identical to $Q4$ with the exception that the volumetric strain energy is integrated using single-point rather than two-point iterated Gaussian quadrature, still an exact evaluation of the element area is obtained.

The vertical tip displacement $u_2(L, 0)$ normalized with respect to the exact solution is presented in Table 1 for $\nu = 0.3$. The same information is provided in Table 2 for a material with $\nu = 0.499$. Notice that the calculated tip displacement is the most accurate for element types $UT3^1$ and $UT3^2$ for all values of n. It is evident from Table 2 that element types $T3$ and $Q4$ behave much too stiffly for values of ν near $1/2$. In contrast, element types $UT3$ and $SQ4$ do not suffer from volumetric locking for this problem. The poor performance of element types $T3$ and $Q4$ becomes even more pronounced as ν approaches the limiting value of $1/2$.

13

Plots of the energy norm of the error are shown in Figure 4 for $P = 1$, $E = 10^7$ and $\nu = 0.3$. The same information is presented in Figure 5 for $\nu = 0.499$. Notice that the results for $UT3^1$ and $UT3^2$ are consistently better than the others. Moreover, the slopes of the line segments for $UT3^1$ and $UT3^2$ are greater than unity. Slopes near unity are characteristic of the asymptotic convergence rate of elements using linear or bilinear shape functions.

The fact that the slopes in Figures 4 and 5 are greater than unity for UST^1 and UST^3 is remarkable since linear interpolation functions are used to calculate the uniform strains of the elements. Such behavior indicates that at least some of the nodes in the mesh exhibit superconvergent behavior for the strains. That is, strains calculated at the nodes converge at a rate higher than that for elements based on linear interpolation functions.

In order to investigate the superconvergent behavior further, it is useful to define the energy norm of the error at the nodes as

$$e_n = \left[(\epsilon^{fe} - \epsilon^{exact})^T D (\epsilon^{fe} - \epsilon^{exact}) \right]^{1/2} \tag{53}$$

Nodes with coordinates $(L/2, c)$, $(L/2, 3c/4)$ and $(L/2, c/2)$ are designated by p_1, p_2 and p_3, respectively. Plots of e_n are shown in Figures 6 and 7 for these three nodes. Notice that the line segment slopes for p_2 and p_3 appear to be approaching an asymptotic value of two. In contrast, the line segment slopes for p_1 appear to be approaching unity. These observations support the idea that nodes internal to the mesh can exhibit superconvergent behavior whereas those on the boundary do not. If this is true, one might expect the slopes of line segments in Figures 4 and 5 to approach a value of two for very large values of n. Slopes less than two may also be caused by the the energy norm of the error being dominated by errors at or near the boundary.

14

The second problem is identical to the first with the exception that the vertical dimension c is reduced from 2 to 1/2. The vertical tip displacement $u_2(16, 0)$ normalized with respect to the exact solution is shown in Table 3 for $\nu = 0.499$. As before, the results are the most accurate for element types $UT3^1$ and $UT3^2$. Comparison of Tables 2 and 3 shows an overall reduction in accuracy for all the element types. These reductions, however, are much less pronounced for the uniform strain elements. The stiffer response reported in Table 3 can be attributed to spurious shear stresses associated with shear locking.

4.2 Example 2, Plain Strain Bending Dynamic Analysis

The second example is identical to the first with the exception that all displacement boundary conditions and applied loads are removed. Of particular interest is the circular frequency ω_1 of the first bending mode of the structure. The frequency error e_ω is defined as

$$e_\omega = |\omega_1^{fe} - \omega_1^{exact}| \tag{54}$$

where ω_1^{fe} and ω_1^{exact} are the finite element and exact circular frequencies of the first bending mode. A consistent mass formulation was used for element types $T3$, $Q4$ and $SQ4$. The mass matrix used for $UT3^1$ and $UT3^2$ was identical to that for $T3$. It is noted that use of a lumped mass matrix for $UT3^1$ and $UT3^2$ results in the appearance of non-physical, low-energy, deformation modes mentioned in Section 2. The "exact" solution for this problem was obtained using twelve-node quadrilateral elements with $n = 16$.

Plots of the frequency error are shown in Figure 8 for a problem with dimensions $L = 16$, $c = 2$ and material properties $E = 10^7$, $\nu = 0.499$ and mass density $\rho = 2.6 \times 10^{-4}$. A slope of two is characteristic of the asymptotic rate of convergence of linear elements. Although an asymptotic rate of convergence has not been attained for $UT3^1$ and $UT3^2$, it is clear that

they produce much more accurate results than than element types $T3$ and $Q4$.

4.3 Example 3, Pure Bending

Example meshes for the remaining problems are shown in Figure 9. The meshes are bounded initially by the six faces $x_1 = 0$, $x_1 = h_1$, $x_2 = 0$, $x_2 = h_2$, $x_3 = 0$ and $x_3 = h_3$. The number of element edges in direction i for each mesh is designated by n_i. The tetrahedral meshes are obtained from the hexahedral meshes by decomposing each hexahedron into six tetrahedra.

The third example deals with the classic problem of pure bending. The applied tractions on the face defined by $x_1 = h_1$ are given by

$$\sigma_{11}(h_1, x_2, x_3) = (h_2/2 - x_2) \tag{55}$$

The displacement boundary conditions for the example are specified as

$$u_1(0, x_2, x_3) = u_2(0, 0, 0) = u_3(0, 0, 0) = u_2(0, 0, h_3) = 0 \tag{56}$$

The number of element edges in the three coordinate directions is given by $n_1 = 2n$, $n_2 = 2n$ and $n_3 = n$. Thus, the meshes shown in Figure 8 have $n = 2$.

A problem with dimensions $h_1 = 10$, $h_2 = 5$ and $h_3 = 1$ is considered first. Results are presented for the uniform strain elements with Option 1 ($UT4^1$) and Option 2 ($UT4^2$), the standard four-node tetrahedron ($T4$), the standard eight-node hexahedron with two-point iterated Gaussian quadrature ($H8$), and the eight-node hexahedron with reduced selective integration ($SH8$). Note that element type $SH8$ is identical to $H8$ with the exception that the volumetric strain energy is based on the mean volumetric strain of the element.

The tip displacement $u_2(h_1, h_2/2, h_3/2)$ normalized with respect to the exact solution is presented in Table 4 for $\nu = 0.3$. The same information is provided in Table 5 for a material

16

with $\nu = 0.499$. Notice that the calculated displacement is the most accurate for element type $UT4^2$. Comparison of the two tables shows that the accuracy of the standard four-node tetrahedron $T4$ and eight-node hexahedron $H8$ is diminished for values of ν near $1/2$.

Plots of the energy norm of the error are shown in Figure 10 for a material with $E = 10^7$ and $\nu = 0.3$. The same information is presented in Figure 11 for $\nu = 0.499$. Notice that the results for the uniform strain elements are consistently better than $UT4$ and the other element types. In contrast to the results for Example 4.1, the energy norm of the error for the uniform strain elements appears to have a convergence rate much closer to the other element types. Slopes of unity are not achieved in Figure 11 for $T4$ and $H8$ because of volumetric locking.

Nodes with coordinates $(h_1/2, h_2, h_3/2)$, $(h_1/2, 3h_2/4, h_3/2)$ and $(h_1/2, h_2/2, h_3/2)$ are designated by p_1, p_2 and p_3, respectively. Plots of e_n (see Eq. 53) for the three nodes are shown in Figure 12. Notice that the line segment slopes for p_2 and p_3 are significantly larger than those for p_1. It is clear from the figure that an asymptotic rate of convergence for the three points has not been attained, but the results for nodes internal to the mesh appear to be converging to the exact solution at a rate significantly higher than those for nodes on the boundary. Establishing the asymptotic rate of convergence for p_2 and p_3 requires the extension of Figure 12 to much larger values of n.

The second problem is identical to the first with the exception that the dimension h_2 is reduced from 5 to 1. The tip displacement $u_2(h_1, h_2/2, h_3/2)$ normalized with respect to the exact solution is shown in Table 6 for $\nu = 0.499$. Notice that the results for $UT4^1$ and $UT4^2$ are significantly better than those for the other element types. Comparison of Tables 5 and 6 shows an overall reduction in accuracy for all element types except $UT4^1$ and $UT4^2$. The

17

stiffer response reported in Table 6 for the other three element types can be attributed to spurious shear stresses associated with shear locking.

The effects of shear locking is demonstrated even more clearly in Table 7 for a problem with dimensions $h_1 = 10$, $h_2 = 0.1$ and $h_3 = 0.02$. For this problem the element aspect ratio in the $X_1 - X_2$ plane is 50 to 1. Comparison of Tables 5 and 7 shows an overall reduction in accuracy for all the element types. Nevertheless, these reductions are much less pronounced for the uniform strain elements.

4.4 Example 4, Second-Order Patch Test

The final example considers a problem with specified tractions on all six faces of the mesh. Tractions on the faces are obtained from the stress-strain relation $\sigma = D\epsilon$ where ϵ is the strain associated with the displacement field

$$u_1(x_1, x_2, x_3) = a(x_2^2 + x_3^2 - 2x_1^2 + 2x_1x_2 + 2x_1x_3 + 5x_2x_3) \tag{57}$$

$$u_2(x_1, x_2, x_3) = a(x_3^2 + x_1^2 - 2x_2^2 + 2x_2x_3 + 2x_2x_1 + 5x_3x_1) \tag{58}$$

$$u_3(x_1, x_2, x_3) = a(x_1^2 + x_2^2 - 2x_3^2 + 2x_3x_1 + 2x_3x_2 + 5x_1x_2) \tag{59}$$

Rigid body motion is constrained by the displacement boundary conditions

$$u_1(0,0,0) = 0 \qquad u_2(0,0,0) = 0 \qquad u_3(0,0,0) = 0 \tag{60}$$

$$u_1(0, h_2, 0) = ah_2^2 \qquad u_2(0, 0, h_3) = ah_3^2 \qquad u_3(h_1, 0, 0) = ah_1^2 \tag{61}$$

The number of element edges in the three coordinate directions is specified as $n_1 = n$, $n_2 = n$ and $n_3 = n$. The dimensions for the problem are given by $h_i = 10$ for $i = 1, 2, 3$. The constant a is set equal to 4×10^{-6}.

18

One can confirm that the elasticity solution to the boundary value problem is given by Eqs. (57-59). In addition, the elasticity solution has no volumetric strain. That is,

$$\frac{\partial u_1}{\partial x_1} + \frac{\partial u_2}{\partial x_2} + \frac{\partial u_3}{\partial x_3} = 0 \tag{62}$$

The energy norm of the error is reported in Table 8 for different values of ν with $n = 5$. The same information is presented in Table 9 for $n = 6$. Notice that the errors are the largest for element types $T4$ and $H8$. Moreover, comparison of the tables reveals that increasing the mesh resolution has a smaller effect on improving the accuracy for element types $T4$ and $H8$. The poor performance of these elements in this example can be attributed to volumetric locking. In contrast, the results for element types $UT4^1$, $UT4^2$ and $SH8$ are relatively insensitive to changes in values of ν near $1/2$.

5. Conclusions

A family of uniform strain elements was developed for meshes of three-node triangles and four-node tetrahedra. The accuracy of the uniform strain elements was shown to be significantly better than that of standard three-node triangular or four-node tetrahedral elements. It was also demonstrated that volumetric locking can be avoided without requiring the introduction of additional degrees of freedom. Thus, one of the major shortcomings of the three-node triangle and four-node tetrahedron is overcome. Example problems also showed that the effects of shear locking are much smaller for the uniform strain elements than for other lower-order elements.

Superconvergence of strains at nodes internal to the mesh was observed for a set of examples in two dimensions. Higher rates of convergence were also observed in three dimensions, but the asymptotic rate of convergence was not established clearly. A mathematical analysis

19

of the elements would be useful to provide an explanation for the observed behavior. It is possible that a modified formulation for elements on the mesh boundaries could lead to improved rates of convergence for the entire mesh.

The calculations required to form the stiffness matrix of the uniform strain elements are very similar to those for the standard three-node triangle and four-node tetrahedron. There is, however, greater coupling between degrees of freedom in the assembled stiffness matrix of the entire mesh. Coupling may occur between two nodes in the mesh if a traversal from one node to the other is possible over a single element edge or two connected edges. Although this greater degree of coupling leads to more nonzeros in the assembled matrix, the improvements in accuracy outweigh the additional time required for matrix factorization.

The initial results from this study are promising, but additional applications to other problems is needed to understand fully the strengths and weaknesses of the uniform strain elements. We are currently investigating the performance of the elements for problems with geometric and material nonlinearities. Several options are available for the treatment of elements on material boundaries, but these need to be developed and investigated further.

References

1. T. J. R. Hughes, *The Finite Element Method: Linear Static and Dynamic Finite Element Analysis*, Prentice-Hall, Englewood Cliffs, New Jersey, 1987.

2. A. R. Mitchell and D. F. Griffiths, *The Finite Difference Method in Partial Differential Equations*, Wiley, New York, New York, 1980.

3. B. R. Baliga and S. V. Patankar, 'A New Finite-Element Formulation for Convection-Diffusion Problems', *Numerical Heat Transfer*, **3**, 393-409 (1980).

4. R. E. Bank and D. J. Rose, 'Some Error Estimates for the Box Method', *SIAM Journal on Numerical Analysis*, **24**, 777-787 (1987).

5. Z. Cai, 'On the Finite Volume Element Method', *Numerische Mathematik*, **58**, 713-735 (1991).

6. R. Vanselow, 'Relations Between FEM and FVM Applied to the Poisson Equation', *Computing*, **57**, 93-104 (1996).

7. D. P. Flanagan and T. Belytschko, 'A Uniform Strain Hexahedron and Quadrilateral with Orthogonal Hourglass Control', *International Journal for Numerical Methods in Engineering*, **17**, 679-706 (1981).

8. C. R. Dohrmann, S. W. Key, M. W. Heinstein and J. Jung, 'A Least Squares Approach for Uniform Strain Triangular and Tetrahedral Finite Elements', *International Journal for Numerical Methods in Engineering*, **42**, 1181-1197 (1998).

9. S. W. Key, M. W. Heinstein, C. M. Stone, F. J. Mello, M. L. Blanford and K. G. Budge, 'A Suitable Low-Order, 8-Node Tetrahedral Finite Element for Solids', to appear in *International Journal for Numerical Methods in Engineering*.

10. F. P. Preparata and M. I. Shamos, *Computational Geometry: An Introduction*, Springer-Verlag, New York, New York, 1985.

11. C. B. Barber, D. P. Dobkin, and H. T. Huhdanpaa, 'The Quickhull Algorithm for Convex Hulls', *ACM Transactions on Mathematical Software*, **22**, 469-483, (1996).

12. C. R. Dohrmann and S. W. Key, 'A Transition Element for Uniform Strain Hexahedral and Tetrahedral Finite Elements', to appear in *International Journal for Numerical Methods in Engineering*.

Table 1: Normalized tip displacements for Example 4.1 with $L = 16$, $c = 2$ and $\nu = 0.3$.

n	$UT3^1$	$UT3^2$	$T3$	$Q4$	$SQ4$
4	1.0134	1.0082	0.7677	0.9043	0.9162
8	1.0054	1.0037	0.9246	0.9714	0.9750
12	1.0027	1.0020	0.9635	0.9861	0.9880
16	1.0016	1.0013	0.9785	0.9917	0.9929

Table 2: Normalized tip displacements for Example 4.1 with $L = 16$, $c = 2$ and $\nu = 0.499$.

n	$UT3^1$	$UT3^2$	$T3$	$Q4$	$SQ4$
4	1.0094	0.9985	0.5862	0.3338	0.9407
8	1.0045	1.0036	0.7708	0.6328	0.9826
12	1.0023	1.0023	0.8546	0.7845	0.9916
16	1.0014	1.0015	0.8992	0.8612	0.9950

Table 3: Normalized tip displacements for Example 4.1 with $L = 16$, $c = 0.5$ and $\nu = 0.499$.

n	$UT3^1$	$UT3^2$	$T3$	$Q4$	$SQ4$
4	0.9890	0.9725	0.1965	0.2350	0.4979
8	1.0010	0.9994	0.4727	0.5450	0.7960
12	1.0010	1.0005	0.6559	0.7263	0.8964
16	1.0007	1.0005	0.7643	0.8235	0.9383

Table 4: Normalized tip displacements for Example 4.3 with $h_1 = 10$, $h_2 = 5$, $h_3 = 1$ and $\nu = 0.3$.

n	$UT4^1$	$UT4^2$	$T4$	$H8$	$SH8$
2	1.1015	1.0484	0.6834	0.9053	0.9280
4	1.0283	1.0137	0.8901	0.9746	0.9805
6	1.0129	1.0064	0.9465	0.9886	0.9912
8	1.0075	1.0036	0.9687	0.9936	0.9950

Table 5: Normalized tip displacements for Example 4.3 with $h_1 = 10$, $h_2 = 5$, $h_3 = 1$ and $\nu = 0.499$.

n	$UT4^1$	$UT4^2$	$T4$	$H8$	$SH8$
2	1.1058	1.0472	0.4638	0.7455	0.9348
4	1.0290	1.0136	0.6274	0.8293	0.9823
6	1.0135	1.0065	0.7036	0.8802	0.9920
8	1.0079	1.0036	0.7488	0.9142	0.9954

Table 6: Normalized tip displacements for Example 4.3 with $h_1 = 10$, $h_2 = 1$, $h_3 = 1$ and $\nu = 0.499$.

n	$UT4^1$	$UT4^2$	$T4$	$H8$	$SH8$
2	1.0185	1.0098	0.1273	0.2910	0.3238
4	1.0212	1.0145	0.3339	0.5740	0.6566
6	1.0114	1.0079	0.4931	0.7249	0.8113
8	1.0069	1.0033	0.6003	0.8110	0.8843

Table 7: Normalized tip displacements for Example 4.3 with $h_1 = 10$, $h_2 = 0.1$, $h_3 = 0.02$ and $\nu = 0.499$.

n	$UT4^1$	$UT4^2$	$T4$	$H8$	$SH8$
2	0.1945	0.1553	0.0016	0.0048	0.0048
4	0.7616	0.6523	0.0063	0.0188	0.0188
6	0.9249	0.8735	0.0141	0.0412	0.0414
8	0.9710	0.9465	0.0246	0.0708	0.0713

Table 8: Energy norm of the error for Example 4.4 with $n = 5$.

ν	$UT4^1$	$UT4^2$	$T4$	$H8$	$SH8$
0.40000	2.3396	2.3278	4.6309	2.3798	1.2771
0.49000	2.2740	2.2582	6.0322	5.0768	1.2403
0.49900	2.2682	2.2517	6.5912	7.5066	1.2368
0.49990	2.2676	2.2511	6.6744	8.0389	1.2364
0.49999	2.2676	2.2510	6.6832	8.0992	1.2364

Table 9: Energy norm of the error for Example 4.4 with $n = 6$.

ν	$UT4^1$	$UT4^2$	$T4$	$H8$	$SH8$
0.40000	1.9422	1.9265	4.0547	1.9943	1.0680
0.49000	1.8861	1.8683	5.6178	4.4775	1.0368
0.49900	1.8809	1.8629	6.3465	7.2394	1.0339
0.49990	1.8804	1.8623	6.4681	7.9761	1.0336
0.49999	1.8804	1.8623	6.4813	8.0638	1.0335
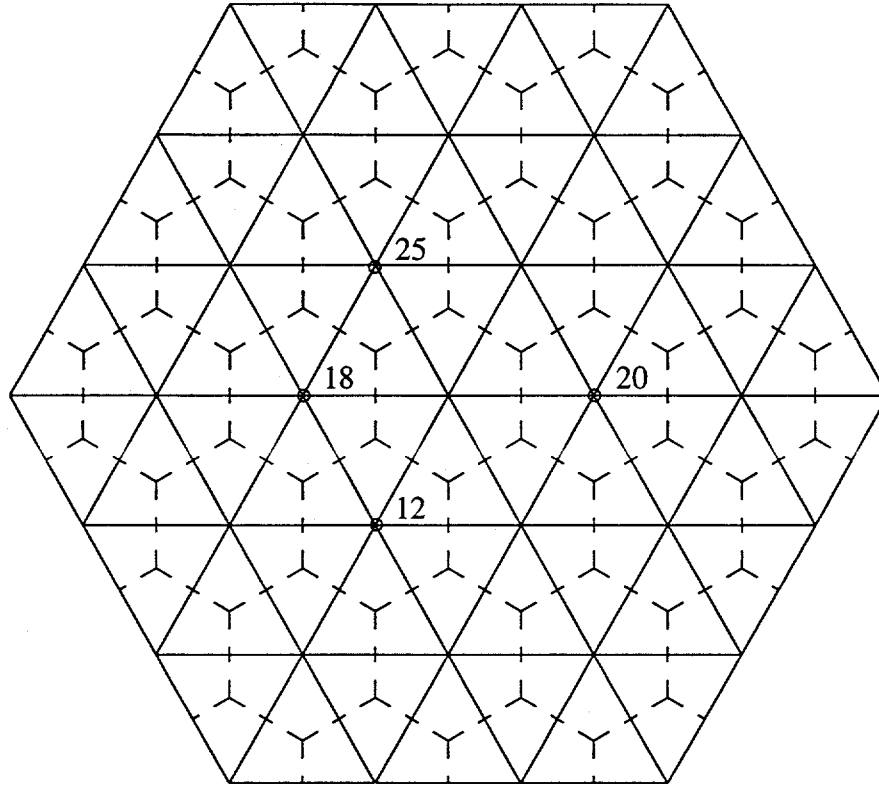
Figure 1: Mesh of three-node equilateral triangles. The dashed lines are formed by perpendicular bisectors of the triangle edges and serve as element (cell) boundaries.
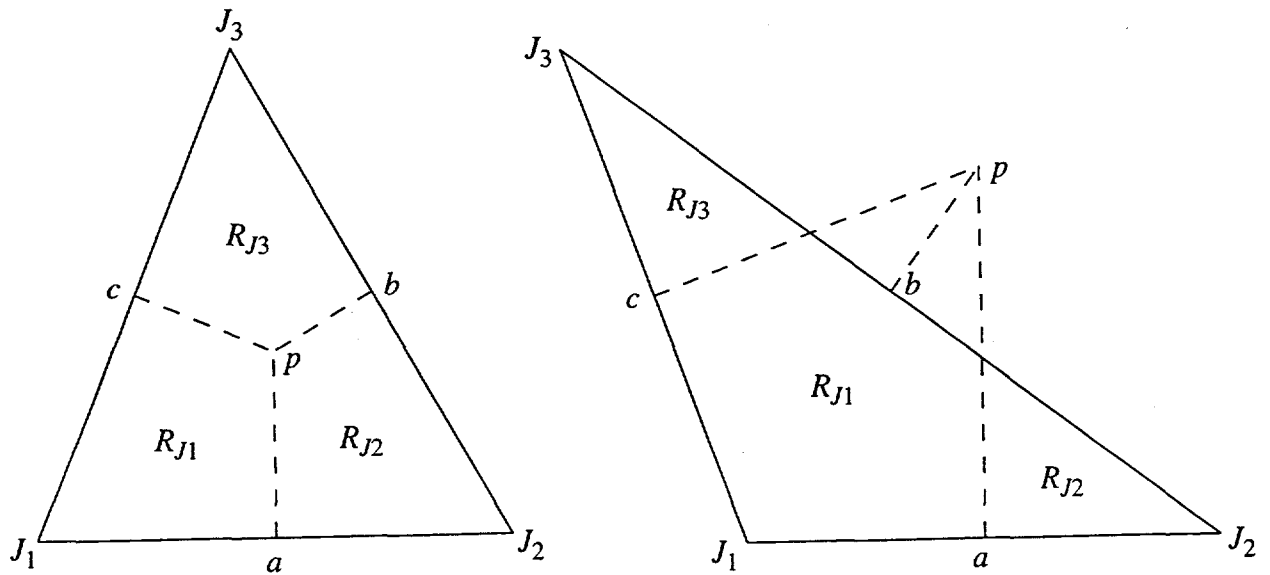
Figure 2: Point p is located at the intersection of the perpendicular bisectors of the triangle edges and is equidistant from J_1, J_2 and J_3. All points within region R_{Jk} are closer to node J_k than to the other two nodes.
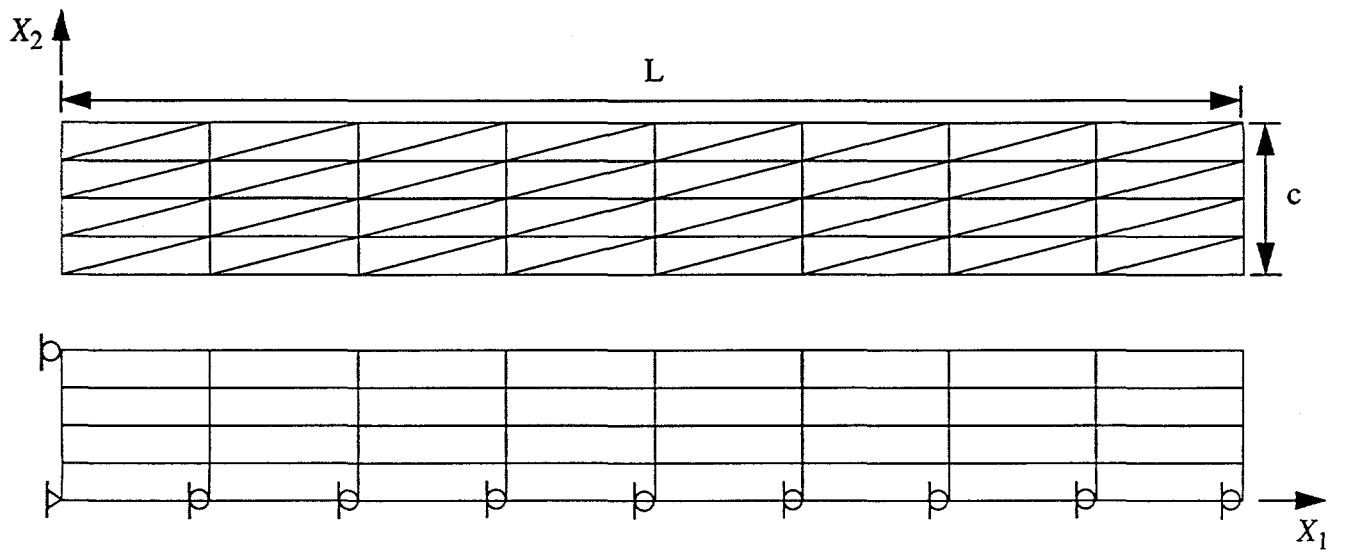
Figure 3: Triangular and quadrilateral meshes for Example 4.1. Both meshes in the figure have $n = 4$.
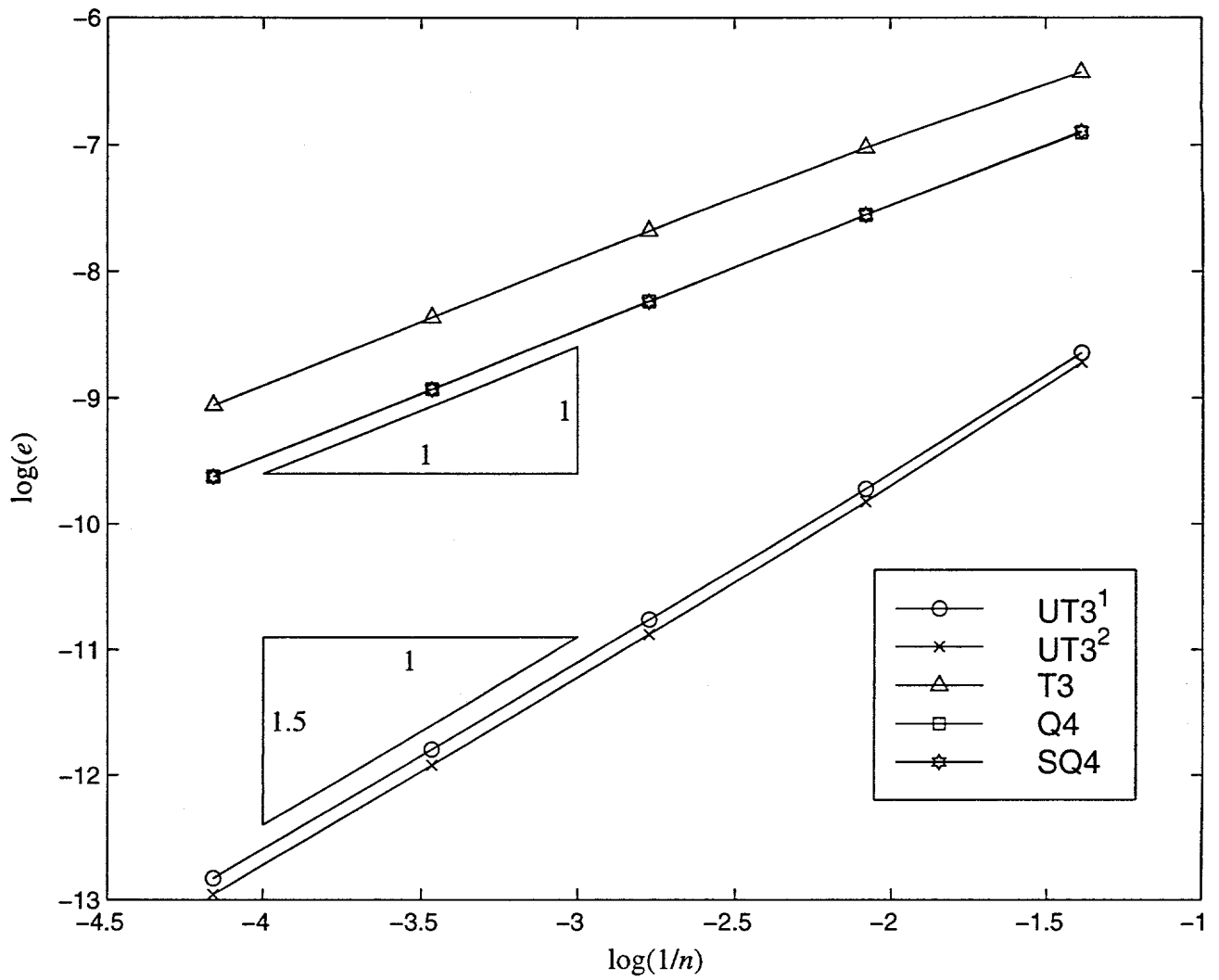
Figure 4: Energy norm of the error for Example 4.1 with $L = 16$, $c = 2$, $P = 1$, $E = 10^7$ and $\nu = 0.3$.
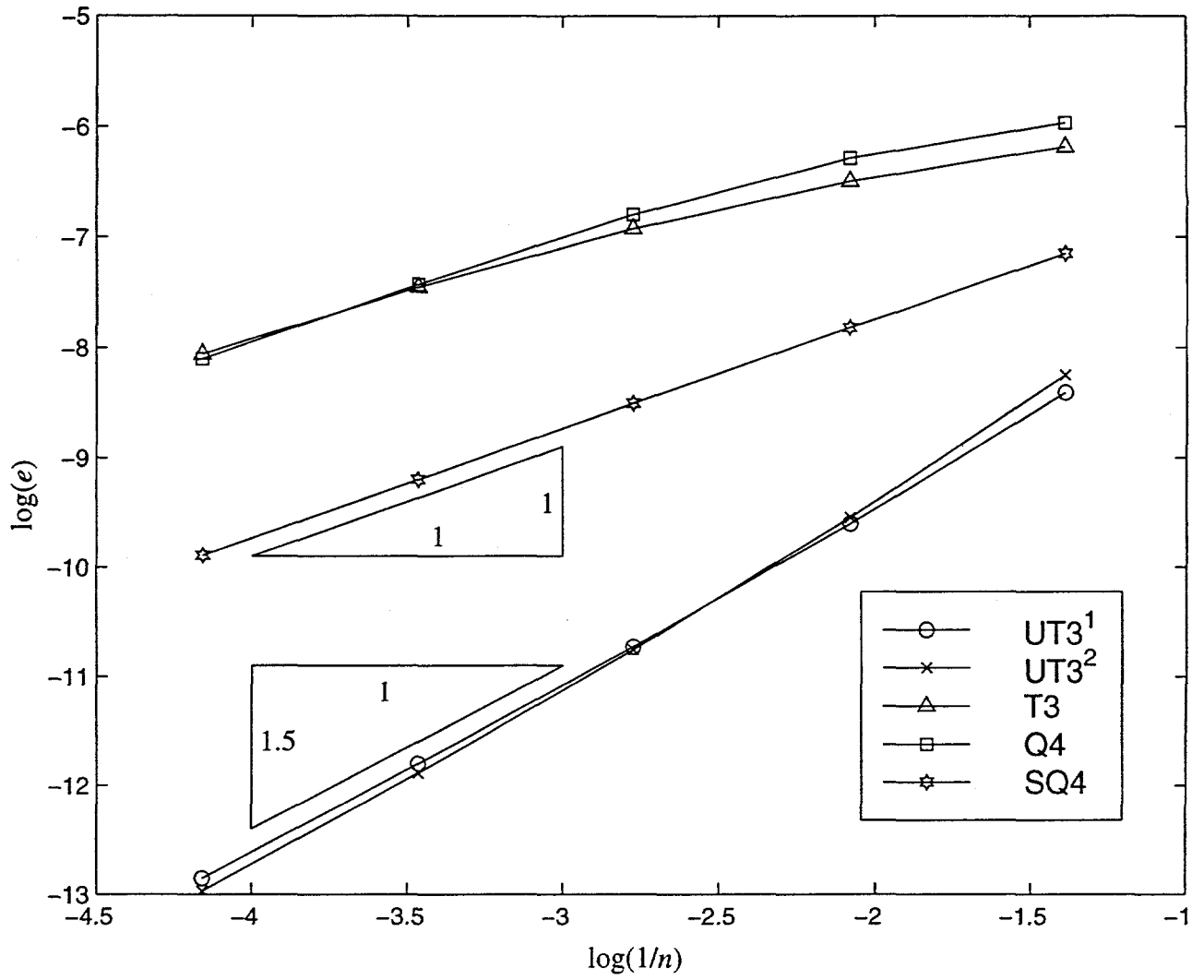
Figure 5: Energy norm of the error for Example 4.1 with $L = 16$, $c = 2$, $P = 1$, $E = 10^7$ and $v = 0.499$.
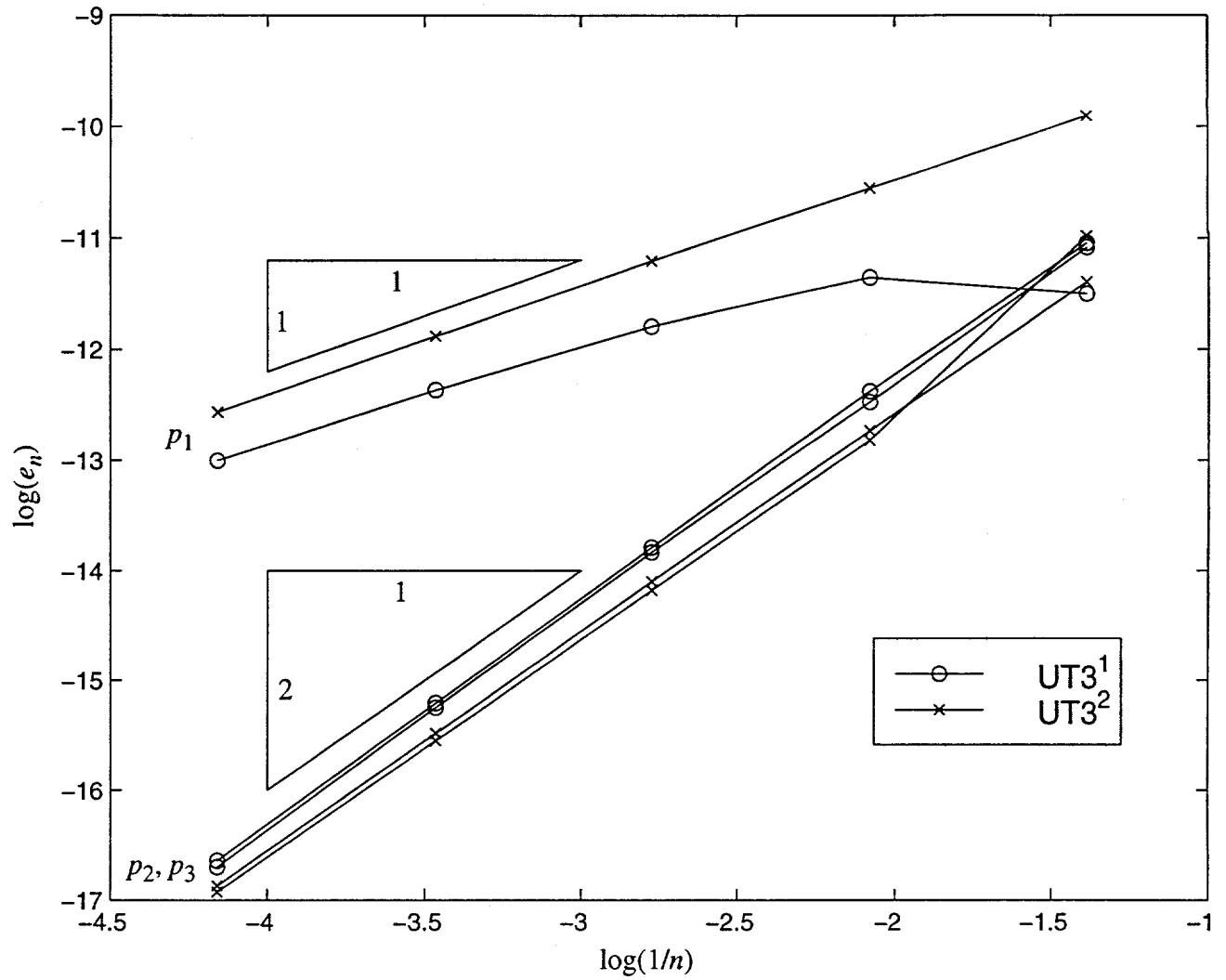
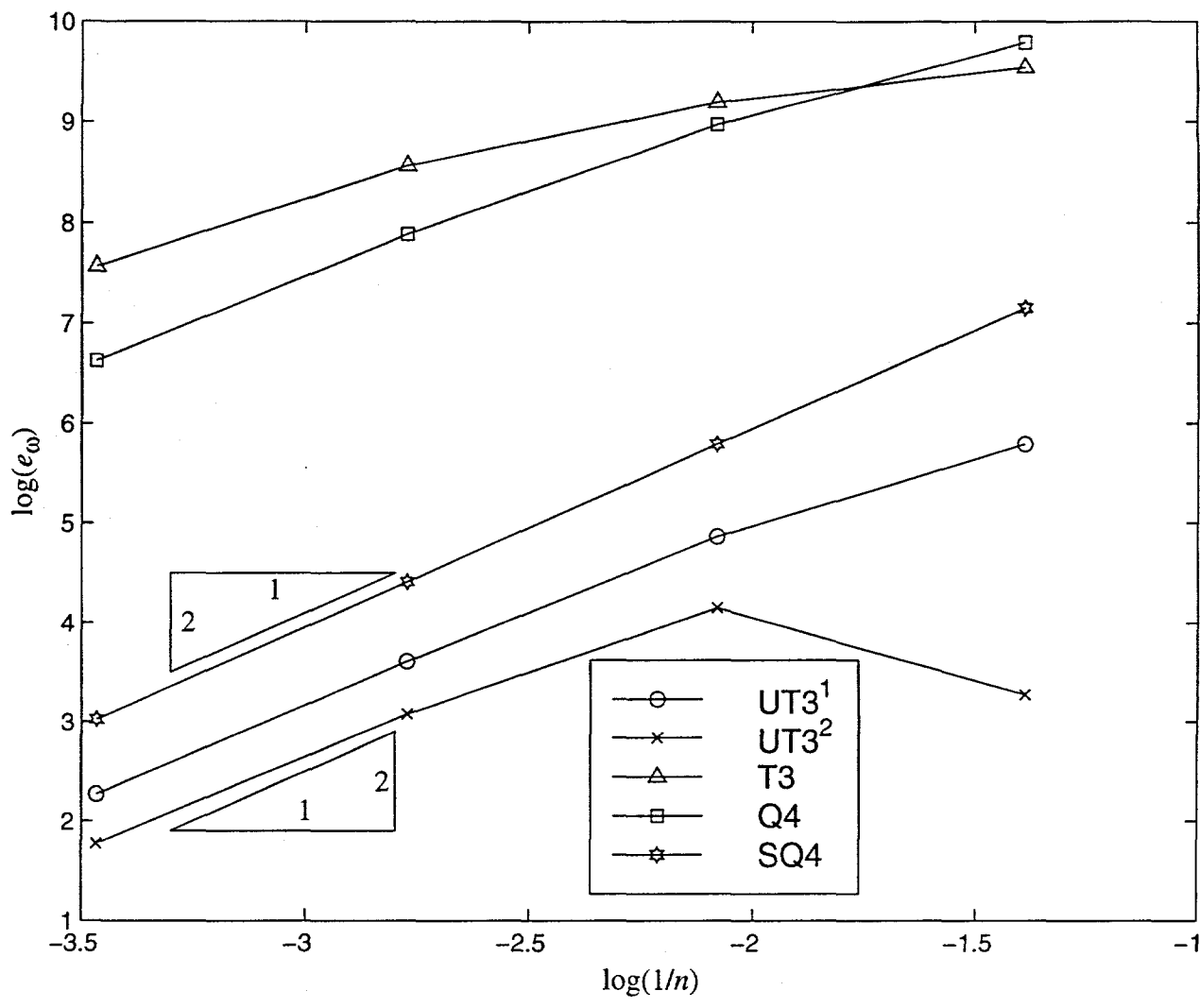Figure 6: Energy norm of the error at nodes p_1, p_2 and p_3 for Example 4.1 with $L = 16$, $c = 2$, $P = 1$, $E = 10^7$ and $\nu = 0.3$.
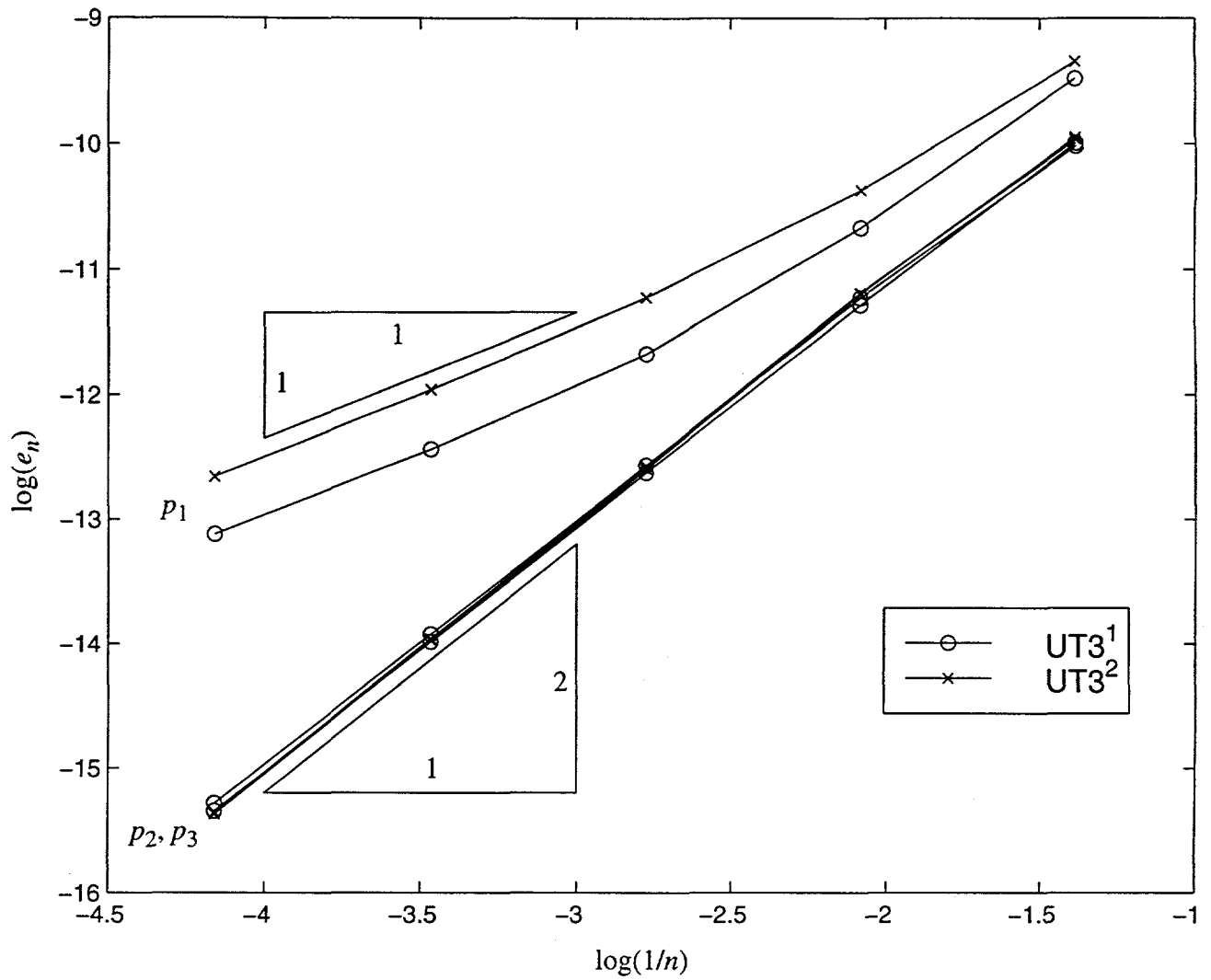
Figure 7: Energy norm of the error at nodes p_1, p_2 and p_3 for Example 4.1 with $L = 16$, $c = 2$, $P = 1$, $E = 10^7$ and $\nu = 0.499$.

Figure 8: Frequency error for Example 4.2 with $L = 16$, $c = 2$, $E = 10^7$, $\nu = 0.499$ and $\rho = 2.6 \times 10^{-4}$.
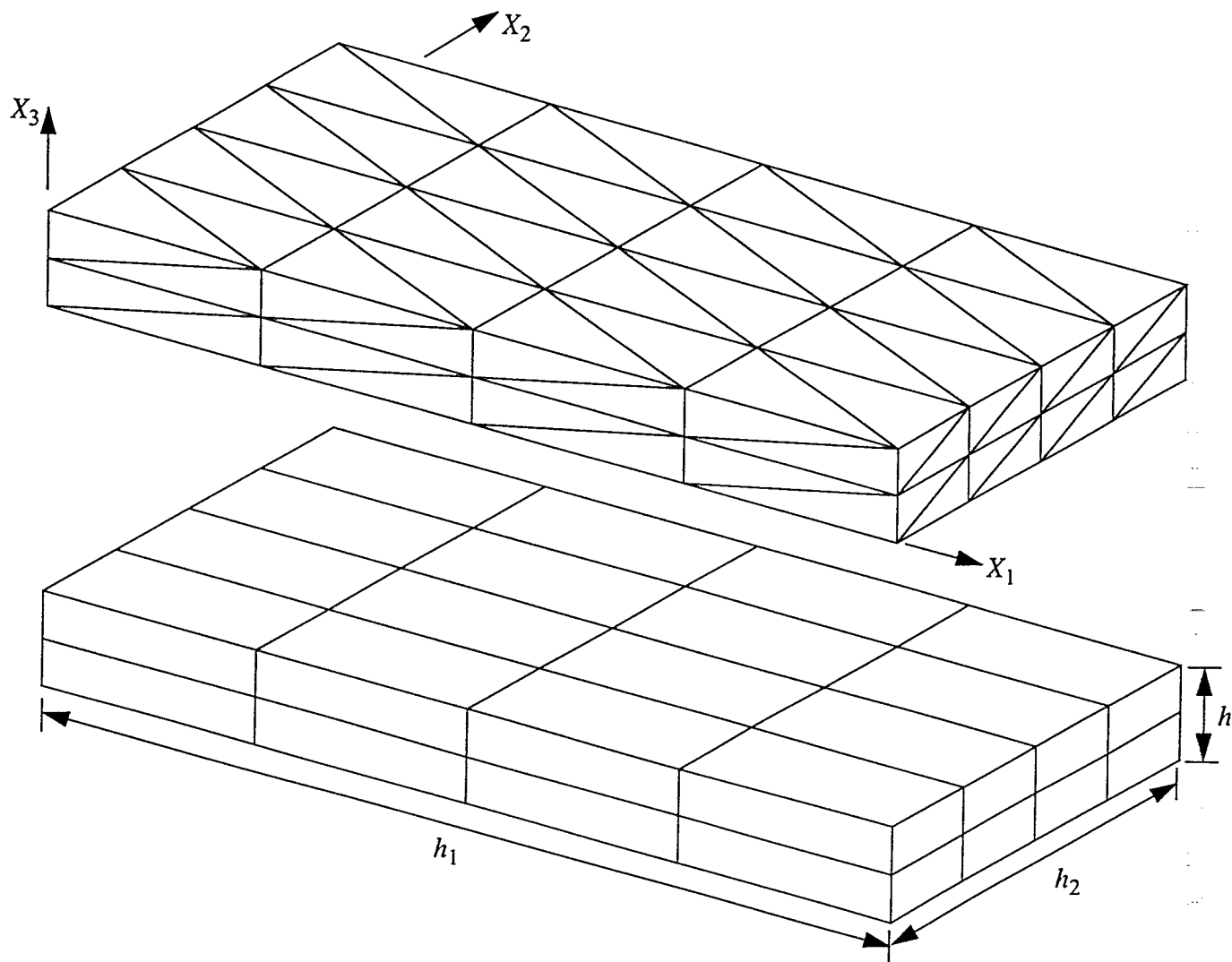
Figure 9: Tetrahedral and hexahedral meshes for Examples 4.3 and 4.4. Both meshes in the figure have $n_1 = 4$, $n_2 = 4$ and $n_3 = 2$.
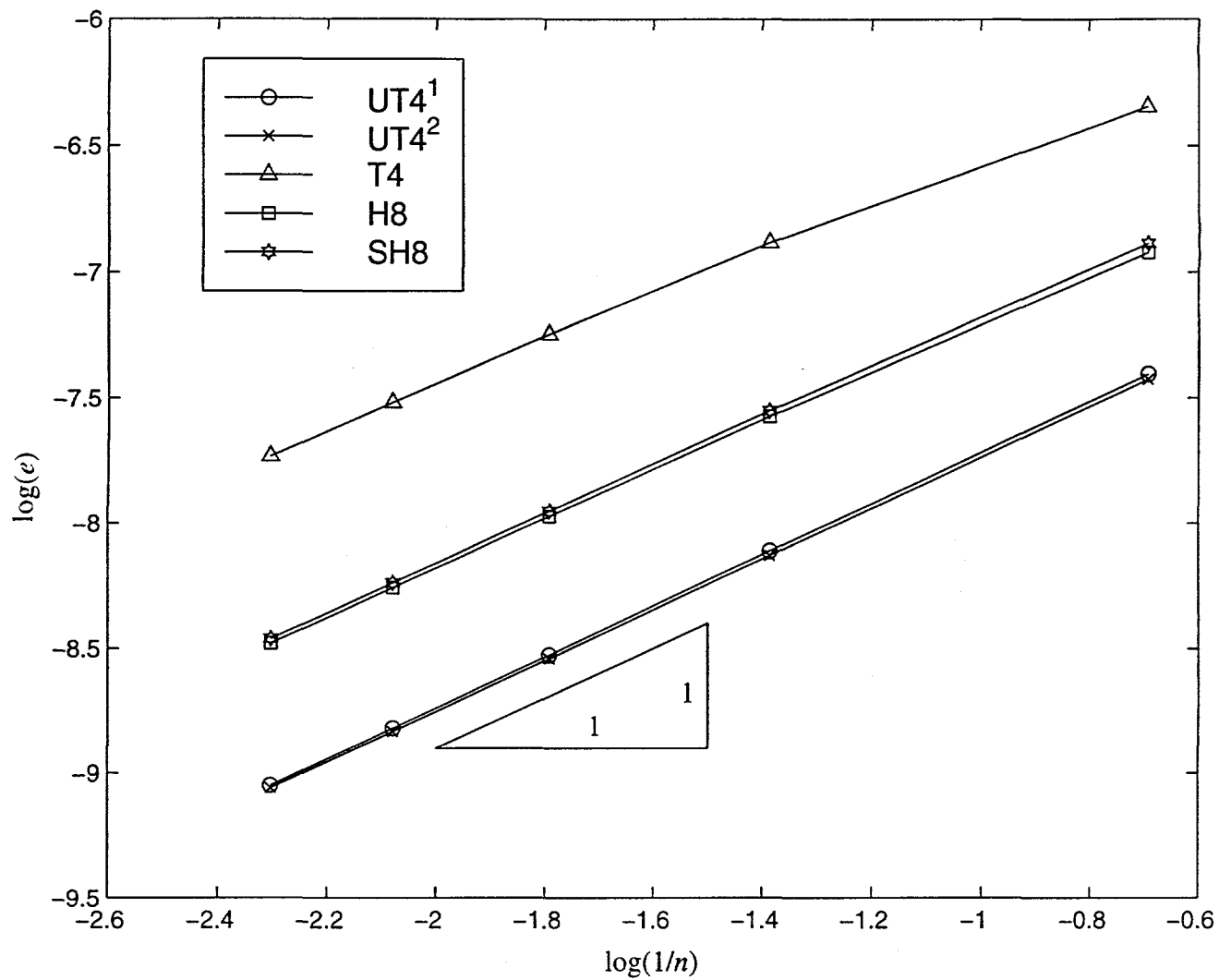
Figure 10: Energy norm of the error for Example 4.3 with $h_1 = 10$, $h_2 = 5$, $h_3 = 1$, $E = 10^7$ and $\nu = 0.3$.
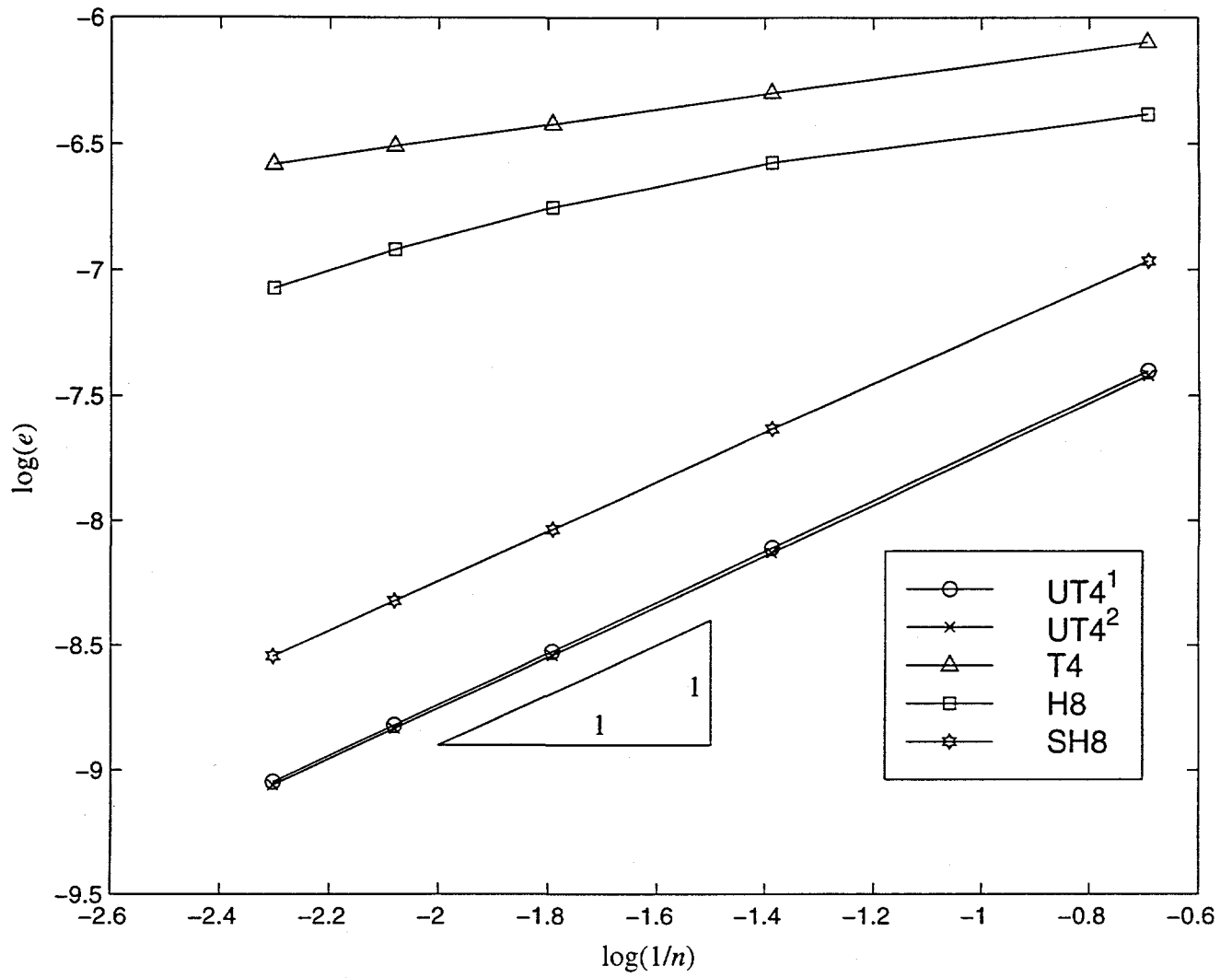
Figure 11: Energy norm of the error for Example 4.3 with $h_1 = 10$, $h_2 = 5$, $h_3 = 1$, $E = 10^7$ and $\nu = 0.499$.
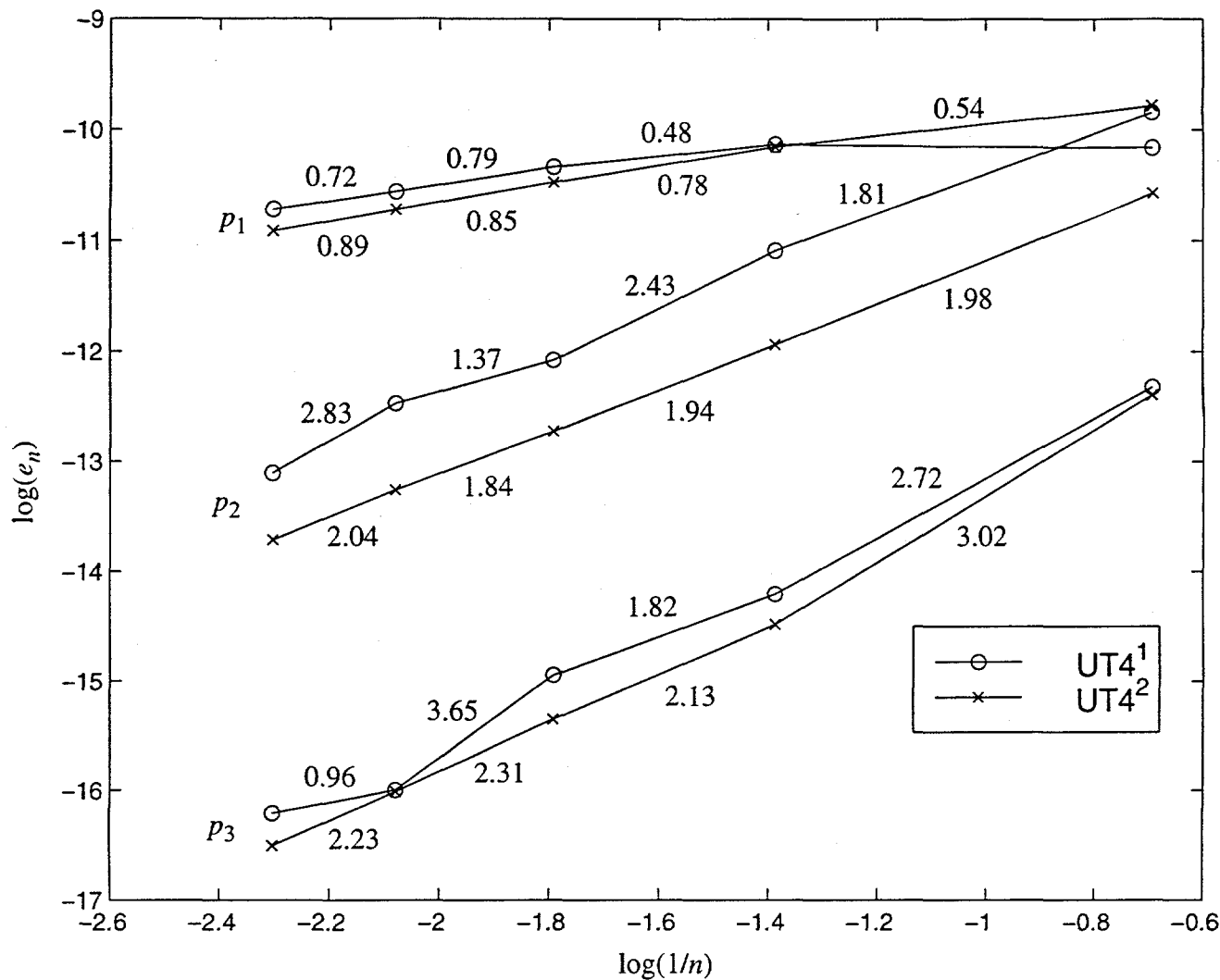
Figure 12: Energy norm of the error at nodes p_1, p_2 and p_3 for Example 4.3 with $h_1 = 10$, $h_2 = 5$, $h_3 = 1$, $E = 10^7$ and $v = 0.3$. Line segment slopes are shown adjacent to the segments.